Influence of Heat Input on Microstructure and Mechanical Properties of Laser Weld Metal in 2507 Duplex Stainless Steel by Different Welding Speed and Welding Power

Shuai ZHAO *, Yaxuan BI

Department of Mechanical Engineering, Hebi Polytechnic, 5 Chaoge Rd., Hebi, Henan, 458030 China
Hebi Institute of Engineering and Technology, Henan Polytechnic University,5 Chaoge Rd., Hebi, Henan, 458030 China

https://doi.org/10.5755/j02.ms.34338

Received 8 June 2023; accepted 8 August 2023

This manuscript attempts to explore the macroscopic morphology microstructural aspects and mechanical properties of different laser welding speed and power on the 2.5 mm thick DSS welding joint. Through the evaluation of 12 groups samples with different welding parameters, we found that the optimal laser welding process parameters were a welding speed of 6mm/s, laser power of 1.6 kW and welding speed of 8 mm/s, laser power of 1.7 kW. When the heat input was 2.125 kJ/cm, the content of ferrite and austenite was relatively uniform, and the ratio was close to 1:1. We found that the hardness of the weld metal zone was slightly higher than that of the base metal, with an average value of 330 HV. When the heat input was 2.125 kJ/cm, the microhardness of welded joint was better than other parameters, reaching 400 HV in the welding metal zone. The tensile strength of the weld was enhanced with the increase of heat input, and the maximum was 900 MPa. Through SEM analysis, the fracture locations of tensile specimens were all in the weld zone, and the fracture morphology had a large number of dimples, belonging to the ductile fracture.
Keywords: 2507 duplex stainless steel, laser welding, microstructure, mechanical properties.

1. INTRODUCTION

Duplex stainless steel (DSS) consists of nearly equal amounts of ferrite and austenite phases at room temperature, and the content of the phase needs to reach at least 30 % stainless steel [1, 2]. DSS can combine the characteristics of austenitic stainless steel and ferritic stainless steel. So DSS has excellent mechanical properties, corrosion resistance and fatigue resistance, and is widely used in environments where the strength and corrosion resistance of materials are demanding, such as shipbuilding, petrochemical, military industry, seawater desalination and other fields [3 – 5]. Compared with DSS 2101 and DSS 2205, DSS 2507 has significantly improved strength and corrosion resistance with the increase of Cr, Mo and N content, especially suitable for organic and inorganic acid environments containing Cl.

In practical application, due to the rapid heating and cooling of the welding process, DSS 2507 microstructure often produces phase imbalance, harmful secondary phase precipitation and other problems. Therefore, domestic and foreign scholars have carried out a series of research work on DSS 2507 welding methods. Makhdoom et al. showed that the mechanical properties and corrosion resistance of shielded metal arc welding (SMAW) were lower than that of gas tungsten arc welding (GTAW) [6]. Devendranath et al. studied the welding process of 5 mm 2507 DSS using 1.17 kJ/mm GTAW with heat input [7]. Cervo et al.welded 2507 DSS by SMAW and conducted post-weld heat treatment, and studied the influence of annealing temperature on welded joints [8]. However, the above conventional welding methods, on the one hand, will cause uneven distribution of microstructure, grain coarsening, imbalance of two-phase ratio, brittle phase precipitation, etc. [9] and reduce the mechanical properties and corrosion resistance of the joint. On the other hand, due to the large welding equipment, the larger groove is needed for welding structural parts, which increases the internal stress of welded joints [10]. Plasma arc welding (PAW), electron beam welding (EBW) and laser beam welding (LBW) belong to high energy density welding methods, which have the advantages of fast welding speed, high production efficiency, small welding deformation and no need to fill metal, etc., suitable for the one-time welding forming of DSS plate. Hong et al. found that when PAW was used to weld DSS, the ferrite content in the weld and heat-affected zone exceeded 70 %, and the two-phase ratio was seriously unbalanced [11]. Taban et al. carried out DSS 2507 with two different heat inputs of 1.90 kJ/mm and 2.25 kJ/mm by PAW and studied the influence of welding heat input on the microstructure and low temperature toughness of the welded joint [12, 13]. Ramkumar et al. found that EBW could achieve one-time penetration of 6 mm DSS, and the two-phase ratio in the weld could be controlled within a reasonable range, but the ferrite content in the weld was higher compared with the base material, and EBW needed to be carried out under vacuum condition, which may lead to more N loss and further inhibit austenite formation in the

* Corresponding author. Tel.: +86-15139237027.
E-mail: *zhaos@hup.edu.cn* (S. Zhao)

weld [14]. Kolenic et al. used different heat input to perform laser welding on 2507 DSS and found that the increase of heat input could reduce the ferrite content in the weld, and the adjustment of welding heat input could obtain a laser welded joint with a reasonable two-phase ratio [15]. Metelkova et al. made the upper part of the weld gradually narrow and shorten by changing the focus position of the beam, and the number of pores in the weld decreased significantly [16]. Saravanan et al. conducted post-weld heat treatment on the welded joints of DSS 2507 with different heat input, and found that austenite content increased in the weld with the increase of heat input and post-weld heat treatment could significantly reduce the ferrite content in the weld, balance the two-phase ratio and improve the pitting resistance of the welded joints [17]. Compared with PAW and EBW, LBW is an efficient and precise welding method, which uses a focused laser beams as energy to blast the weldment. It has the advantages of fast welding speed, concentrated heating, small HAZ, and large depth to width ratio [18 – 21]. However, in the process of the thin type DSS welding, it is easy to appear an uneven distribution of microstructure and grain coarsening [22]. The base metal plate is thin, and the weld is easy to produce internal stress [23]. Shao et al. pointed out that in the welding process, Cr, Mo, and other alloying elements are easy to oxidize, forming inclusions, and forming carbides with C element, which will seriously affect the weld performance [24]. Wang et al. found that the adoption of appropriate technology can avoid weld inclusions and oxide formation, and the weld shape was good, but the phase proportion in the weld microstructure was seriously maladjusted [25]. Li et al. found that small heat input during laser welding would lead to excessive ferrite content in the weld, and the toughness of the welded joint would decrease [26]. Therefore, controlling the two-phase proportion in the process of the thin type DSS welding, to ensure the mechanical properties and corrosion resistance, was the key problem that needs to be further studied and solved in the current laser welding field [27]. On the basis of combing the research results of domestic and foreign scholars, this manuscript with 1.5 mm thick 2507 DSS as the research object, adopted the laser welding method under different laser power and welding speed, respectively through morphology observation, microstructure analysis and mechanical properties, providing the theoretical basis and data support for laser welding process of DSS 2507.

2. MATERIALS AND METHODS

The test materials were flat plates with a thickness of 1.5 mm made of DSS 2507, which were in the solid solution state at room temperature. The chemical composition of the used steels was showed in Table 1. Before the welding test, the joint surface of the welding test plate was polished with 500# sandpaper to remove the oxide film on the surface, and the welded joint was welded by the docking method, as shown in Fig. 1 a. The experimental equipment was YLS-6000-S2T fiber laser welding system, the single-point laser energy was 25 J, the laser wavelength was 1070 mm. The fiber core diameter was 200 μm, the beam diameter was 0.5 mm, laser intensity was 3×10^6 W/cm^2, the laser pulse width was 10 ms, the defocus amount was 0.5 mm, the focal length was 310 mm, the focal diameter was 0.29 mm, and the protective gas flow rate was 6 L/min.

Table 1. Chemical composition of DSS 2507

Chemical composition, wt.%								
C	Si	Mn	P	S	Cr	Ni	Mo	N
≤0.03	≤0.8	≤1.2	≤0.035	≤0.02	24 – 26	6 – 8	3 – 5	0.24 – 0.32

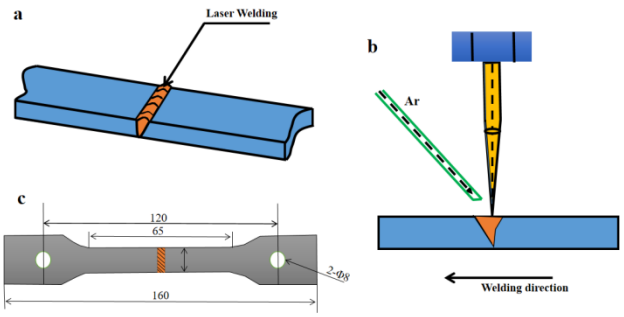

Fig. 1. a – schematic of the laser butt joint; b – schematic of laser welding; c – size of the tensile sample, mm

Argon was selected as the protective gas, and the surface of the workpiece was blown at an Angle of about 45°, as shown in Fig. 1 b. In the process of laser welding, welding power is closely related to the number of pores. With the increase of laser power, the number of pores increases, because the increase of laser power can promote the formation of metal vapor, which leads to the formation of pores [28], but low welding power will lead to small penetration. Therefore, the foundation welding power is 1.5 kW used in this study. When the laser power is constant, the welding speed has a great impact on the shape of the weld pool and weld. If the welding speed is too low, it will lead to strong vaporization or welding penetration of the material. If the welding speed is too high, the weld may not be penetrated, and the joint performance becomes worse. Therefore, it is very important to obtain a reasonable welding speed, and the basic welding speed was 4 mm/s. In this study, the control variable method was adopted to conduct welding tests. After the welding speed was determined to be 4 mm/s, experiments were conducted in sequence according to the different power. The specific laser welding process parameters and experiment sequence were shown in Table 2.

Table 2. Design of laser welding process

Welding speed	Laser power		
	1.5 kW	1.6 kW	1.7 kW
4 mm/s	1	2	3
6 mm/s	4	5	6
8 mm/s	7	8	9
10 mm/s	10	11	12

After welding, the samples were ground, polished, and corroded. OLYMPUS optical microscope (OM) was used to observe the forming condition and morphology of the weld. HITACHI S-3400N scanning electron microscope (SEM) was used to analyse the microstructure of the weld. The hardness of the samples was tested by JMHVS-1000AT hardness tester. The tests were taken on the fusion line of the weld as the origin and were carried out to both ends. The load was 100 g, the pressure holding time was 20 s, the

adjacent test point was 0.1 mm around the weld, and the area far from the weld was tested by a non-equal interval method. A 300kN SHT4305 electronic universal testing machine was used to test the tensile strength according to the "GB/T2651-2008 Tensile test Method for Welded joints". The tensile sample was processed in Fig. 1 c, and the microstructure at the fracture of the tensile sample was observed by SEM.

3. RESULTS

3.1. Macromorphology observation

In the welding test, the laser power was set to 1.5 kW, 1.6 kW, and 1.7 kW, respectively, at the speed of 6 mm/s. The macromorphology of the front and back sides of the weld were shown in Fig. 2. The change of laser power had a great influence on the forming state of the joint surface, and the weld width increased with the increase of power.

On the front side, the weld metal was brighter than the base metal due to the presence of protective gas. when the power was too high, the original protective gas flow was difficult to meet the requirements, and the fish scale pattern was staggered, which was the clearest in Fig. 2 a, and oxidation occurs in Fig. 2 b and c.

On the back side, Fig. 2 a was not thoroughly welded, Fig. 2 b was thoroughly welded, and Fig. 2 c had a serious oxidation phenomenon due to excessive power. It showed that the steel plate could be gradually welded through with the increase of laser power when the welding speed was constant, but the weld was over oxidized and the formability was reduced when the power was greater than a certain optimal value. The quality of the front weld of Fig. 2 a is better than that of Fig. 2 b, but the back side of Fig. 2 a is not penetrated, which will lead to the decline of the strength of the welded joint.

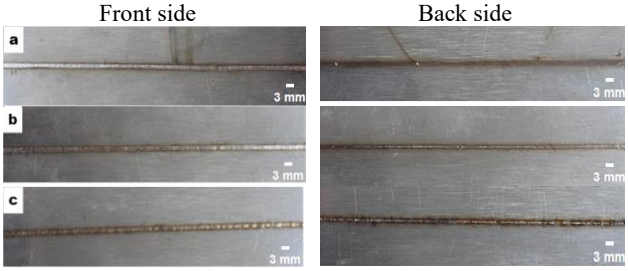

Fig. 2. Macromorphology of the weld: a – welding speed 6 mm/s, welding power 1.5 kW; b – welding speed 6 mm/s, welding power 1.6 kW; c – welding speed 6 mm/s, welding power 1.7 kW

Therefore, the forming quality of Fig. 2 b is better than that of Fig. 2 a by comprehensive comparison. The worst joint quality is in Fig. 2 c. So, 1.6 kW was a reasonable laser power at the welding speed of 6 mm/s.

In the welding test, the welding speed was set to 4 m/s, 6 mm/s, 8 mm/s, and 10 mm/s respectively, at a laser power of 1.7 kW, and the macromorphology of the front and back sides of the weld were shown in Fig. 3. On the front side, the change of welding speed had a great influence on the forming state of the joint surface, and the width of the weld decreased with the increase of welding speed, and the brightness of the weld metal increased with the increase of the welding speed. because the required protection gas was reduced when the welding speed increased, and the protection gas flow was certain, so the anti-oxidation effect was good.

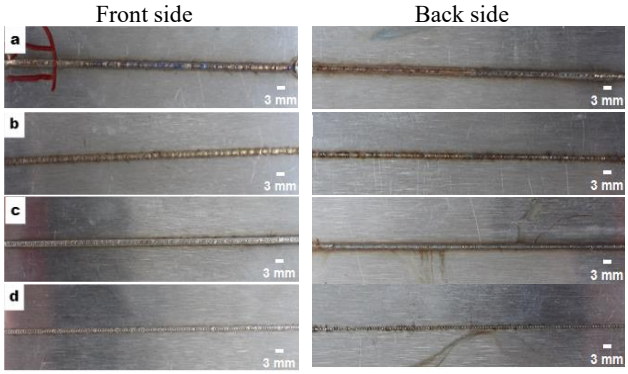

Fig. 3. Macromorphology of the weld: a – welding speed 4 mm/s, welding power 1.7 kW; b – welding speed 6 mm/s, welding power 1.7 kW; c – welding speed 8 mm/s, welding power 1.7 kW; d – welding speed 10 mm/s, welding power 1.7 kW

In Fig. 3 c and d, the scale pattern of fish was clear, and the layers were staggered. In Fig. 3 a and b, the weld was oxidized and the inter layer was blurred. On the back side, the steel plate in Fig. 3 a – c was fully welded, and the steel plate in Fig. 3 d was not thoroughly welded. However, the weld in Fig. 3 a and b had different degrees of oxidation phenomenon due to the low welding speed. This indicated that when the welding power was fixed, the steel plate could be gradually welded through with the decrease of the welding speed, but when the welding speed was less than a certain optimal value, the weld was over-oxidized, resulting in the reduction of formability. It could be seen from Fig. 3 that the forming quality of Fig. 3 c was the best compared with Fig. 3 b, d, and a, that is, 8 mm/s was a reasonable welding speed under the laser power of 1.7 kW.

To study the effect of laser welding parameters on the macromorphology weld, 12 groups of different welding parameters were tested on the samples, as shown in Table 3 and Table 4. Through the analysis of weld macroscopic morphology, the optimal laser welding process parameters are a welding speed of 6 mm/s, laser power of 1.6 kW and welding speed of 8 mm/s, laser power of 1.7 kW.

Table 3. Effect of welding parameters on the macromorphology of the front weld

Welding speed	Laser power		
	1.5 kW	1.6 kW	1.7 kW
4 mm/s	Oxidation	Oxidation	Severe oxidation
6 mm/s	Bright and uniform melting width	Slight oxidation	Oxidation
8 mm/s	Bright and uniform melting width	Bright and uniform melting width	Slight oxidation
10 mm/s	Bright and uniform melting width	Bright, uniform melting width and increased fish scale spacing	Bright, uniform melting width and increased fish scale spacing

To comprehensively analyze the effect of laser welding speed and welding power on the weld performance, this

experiment introduced heat input to measure the joint effect of the two factors. The calculation formula of welding heat input E (kJ/cm) is as follows:

$$E=\eta P/v, \quad (1)$$

where η is the thermal efficiency coefficient; P is the laser power, W; v is the welding speed, cm/s. Here, the effect of η is ignored and the nominal heat input is used:

$$E1=P/v. \quad (2)$$

After converting the experimental parameters into heat input by Eq. 2, as shown in Table 5.

Table 4. Effect of welding parameters on macromorphology of the back weld

Welding speed	Laser power		
	1.5 kW	1.6 kW	1.7 kW
4 mm/s	Incomplete penetration and serious oxidation	Penetration and serious oxidation	Penetration and serious oxidation
6 mm/s	Incomplete penetration and oxidation	Penetration and oxidation	Penetration and serious oxidation
8 mm/s	Incomplete penetration and no oxidation	Incomplete penetration and slight oxidation	Penetration and oxidation
10 mm/s	Incomplete penetration and no oxidation	Incomplete penetration and slight oxidation	Incomplete penetration, spot spacing distribution, slight oxidation

Table 5. Heat inputs corresponding to different process parameters

Welding speed	Laser power		
	1.5 kW	1.6 kW	1.7 kW
4 mm/s	3.75	4	4.25
6 mm/s	2.5	2.67	2.83
8 mm/s	1.875	2	2.125
10 mm/s	1.5	1.6	1.7

3.2 Microstructure analysis

SEM was used to observe the weld with heat input values of 1.7 kJ/cm, 2.125 kJ/cm, 2.83 kJ/cm, and 4.25 kJ/cm, respectively, and the microstructure was shown in Fig. 4. It could be seen from the figure that the welded joint was mainly composed of weld metal zone (WM)and heat affected zone (HAZ). As the temperature was high enough, the transition from solid phase to liquid phase occurred [17]. During the cooling process, more ferrite existed in WM, due to the fast cooling rate. Because the DSS was solidified in ferrite mode, the weld metal will keep the ferrite structure after solidification, and when the temperature was lower than the ferrite transition curve temperature, part of the ferrite phase became austenite. Wang et al. believed that due to the segregation of elements and lattice distortion at the grain boundary, the ability of grain boundary emergence was high, and the driving force required for the transformation of grain boundary ferrite was small [25]. Therefore, austenite in the weld mostly existed as grain boundary austenite. Fig. 4 also proved that ferrite has two morphisms: columnar crystals growing towards the center along the fusion line and equiaxed crystals in HAZ. Ferrite grains grew to the center along the fusion line and showed a columnar crystal shape in WM, because the crystal will preferentially grow perpendicular to the fusion line in the laser welding process. Austenite mainly existed at the grain boundary of ferrite in the weld microstructure. With the increase of heat input, the elongated grain grew clearly, the austenite continuity increased at the grain boundaries, and the width increased slightly. When the heat input was 2.125 kJ/cm, the grain size in Fig. 3 b was relatively uniform, with no obvious large fine grain group. The amount of austenite and ferrite was equivalent, and the area size of the dark area and the light area outside the weld was basically the same. This indicated that the ferrite phase and austenitic phase were controlled in a relatively balanced state, close to a 1:1 phase ratio, under this welding process parameters. Due to the grain size of the weld was relatively uniform, so the weld joint had better mechanical properties, which was also verified in the subsequent experiment. Due to the extremely fast cooling speed of laser welding, HAZ was very narrow, with a width of about 20 – 30 μm. When the heat input was 2.125 kJ/cm (1.7 kW, 8 mm/s), the fusion line was clear. When the heat input was 4.25 kJ/cm (1.7 kW, 4 mm/s), austenite between grains grew into the ferrite grain, showing a width structure. Due to a large amount of heat input, the slow cooling rate of the weld, element segregation and lattice distortion at the grain boundaries, a small driving force for ferrite phase transformation, and austenite nucleation and growth at the grain boundaries. In the welding experiment of 5 mm DSS, Gao et al. found that the microstructure of the weld seam was composed of ferrite parent phase and grain boundary austenite, and there was also a small amount of width austenitic side slat [22].

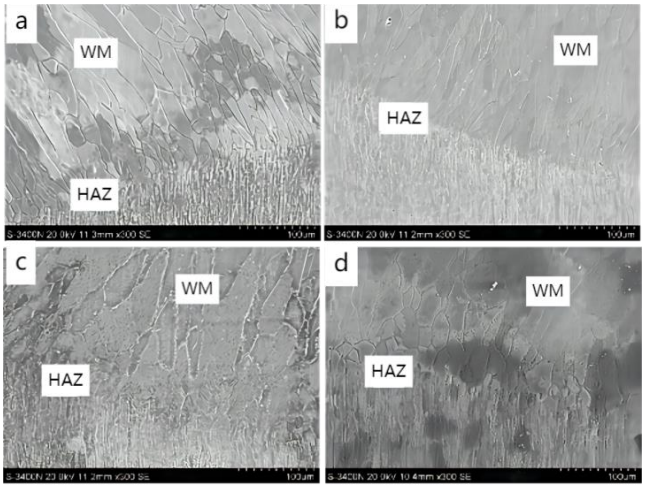

Fig. 4. Microstructure of weld under different heat input: a – 1.5 kJ/cm; b – 2.125 kJ/cm; c – 2.83 kJ/cm; d – 4.25 kJ/cm

3.3. Precipitate analysis

In the rapid cooling process (700 ~ 900 °C) after the completion of welding, due to the large number of ferrites in WZ, the solubility of N in the ferrite decreased sharply, leading to the supersaturated precipitation in the ferrite crystal. Fig. 5 was the SEM image of DSS 2507 after weld corrosion treatment. A large number of pitting pits were

granular and short rod-like, indicating that the nitride precipitates were rod-like or granular. And the location of pitting pits indicated that nitride precipitation mainly occurred in the ferrite grains. By the energy spectrum analysis (EDS)of pitting pits, the results showed that the precipitated phase of nitride in ferrite was chromium nitrogen compound, as shown in Fig. 6.

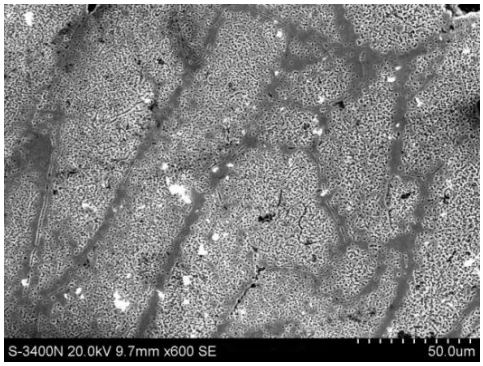

Fig. 5. SEM of Cr_2N distribution in the weld when the heat input is 2.83 kJ/cm

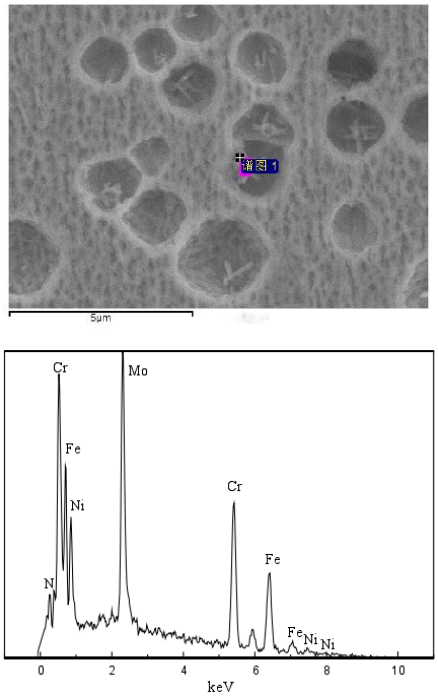

Fig. 6. EDS patterns of precipitated phase

3.4. Mechanical property analysis

As shown in Fig. 7, with the increase of heat input, the weld area also increased correspondingly, but the hardness distribution of the weld was not uniform. When the heat input was 2.125 kJ/cm, the microhardness of the sample reached the maximum 400 HV. Because with the increase of heat input, the microstructure had fine grain size, the distribution of ferrite and austenite were uniform, and the grain boundary areas were increased, leading to greater hindrance to dislocation movement. However, with the further increase of heat input, the grain size and softening degree of this region increased gradually, and the microhardness value decreased gradually. The hardness of the base metal was about 300 HV on average, and the hardness of the WM was not different from that of the base metal, with an average of about 330 HV. Because in the WM, the ferrite content was more than that of the base metal, and the solution strengthening effect caused by N elements in the ferrite increased the hardness of the ferrite. The hardness of the heat-affected zone was the lowest, roughly U-shaped, with an average value of about 280 HV. Because the grain and microstructure coarsened under the influence of heat input, resulting in the lowest hardness.

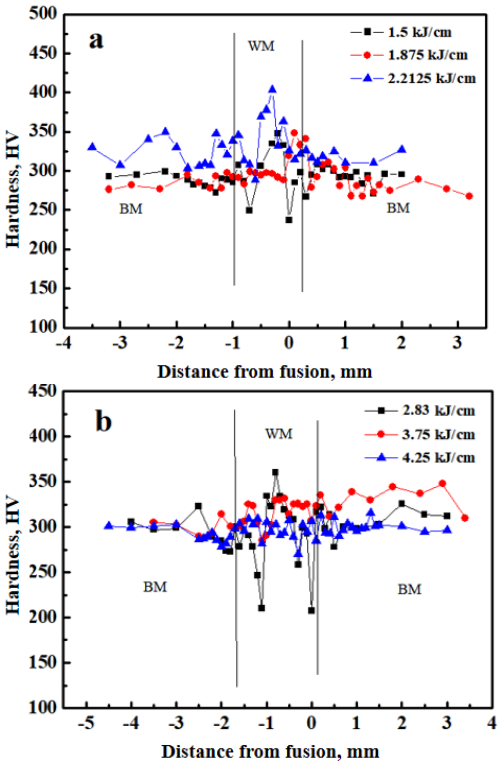

Fig. 7. Hardness curves of welded joints under different heat input: a – heat input at 1.5 kJ/cm, at 1.857 kJ/cm, at 2.125 kJ/cm; b – heat input at 2.83 kJ/cm, at 3.75 kJ/cm, at 4.25 kJ/cm

The specimen was subjected to a tensile test at room temperature, shown in Fig. 8. The tensile properties of samples under different heat inputs were tested and statistically recorded, as shown in Table 6.

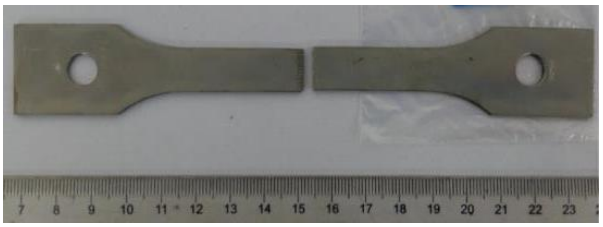

Fig. 8. The image of the tensile tested specimen

Table 6. Average tensile strength (MPa) of sample under different parameters

Welding speed	Laser power		
	1.5 kW	1.6 kW	1.7 kW
4 mm/s	885	–	895
6 mm/s	890	900	885
8 mm/s	790	850	890
10 mm/s	685	800	785

The variation trend was shown in Fig. 9. When the heat input was more than 2.2 kJ/cm, the weld with good tensile strength could be obtained, and the maximum tensile strength was 900 MPa.

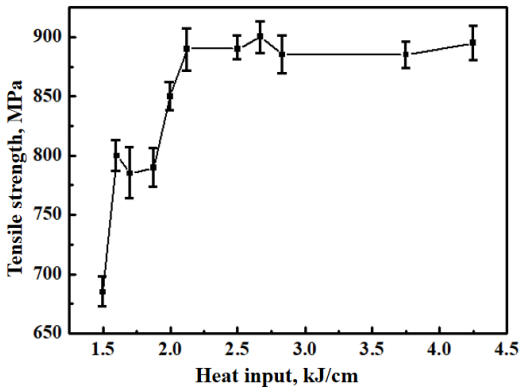

Fig. 9. Average tensile strength of the samples under different heat input

3.5. Tensile fracture analysis

The tensile strength of the joint was reduced due to the softening zone of DSS 2507. In the process of tensile test, plastic deformation occurs preferentially in the softening zone. In the process of the tensile test, plastic deformation occurred preferentially in the softening zone, and a large amount of plastic deformation accumulated in the softening zone, and finally fracture occurs. The macroscopic fracture surface of the sample was dark and fibrous. SEM was used to analyze the fracture morphology of four samples with a heat input of 1.5 kJ/cm, 1.875 kJ/cm, 2.125 kJ/cm, and 2.67 kJ/cm. It is found that there were a lot of dimples in the microscopic fracture of these samples. It can be concluded that the tensile fracture mechanism of DSS 2507 joint belonged to ductile fracture. As shown in Fig. 10, due to the small heat input, most of the welds were not penetrated.

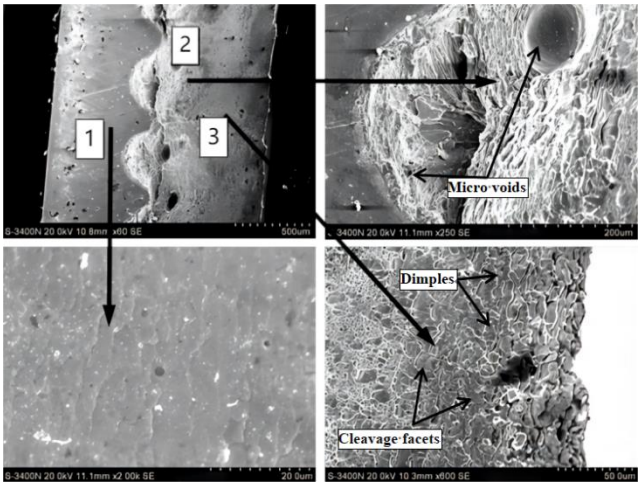

Fig. 10. Fracture morphology of tensile specimens with a heat input of 1.5 kJ/cm

Position 1 was not permeable, but features of the grain boundary appeared, and the elements at the grain boundary were evaporated due to laser heating. Position 2 was the softening zone of the weld, and part of it showed the grain characteristics of the base metal. There were pores in this area, because it took longer for the pores to completely escape with the increase of heat, so the gas in the molten pool accumulated and formed macroscopic pores. Pores in the welds were often the starting point of crack propagation, which reduced the mechanical properties of welded joints and was a serious welding defect. There were many parabolic dimples at position 3, indicating that the toughness of this area was good, which verified that the tensile fracture mechanism of the welded joint was a ductile fracture.

As shown in Fig. 11, the weld part was not permeable, but the area was smaller than that of the sample with a heat input of 1.5 kJ/cm. Position 1 was the impenetrable part, and there were a lot of dimples on the impenetrable edge. There were many parabolic dimples in position 2, indicating that the toughness of this region was good.

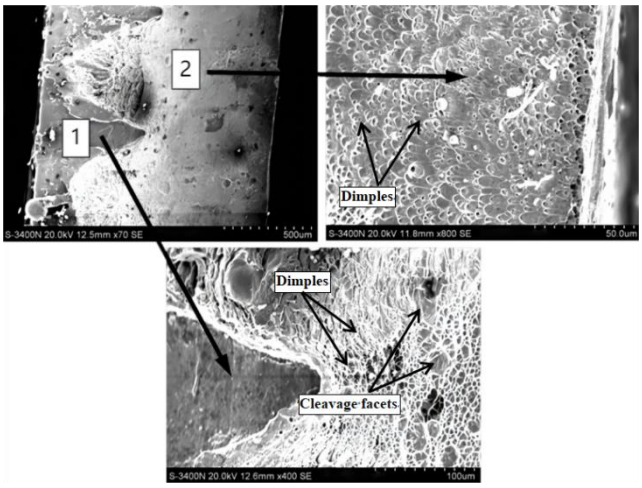

Fig. 11. Fracture morphologies of tensile specimens with a heat input of 1.875 kJ/cm

It can be seen from Fig. 12 that a small part of the weld was not permeable. Position 1 was the part without penetration; position 2 was the softening zone of the weld, with a large number of equiaxial dimples after the fracture, which was a ductile fracture. There were many parabolic dimples in position 3, indicating good toughness.

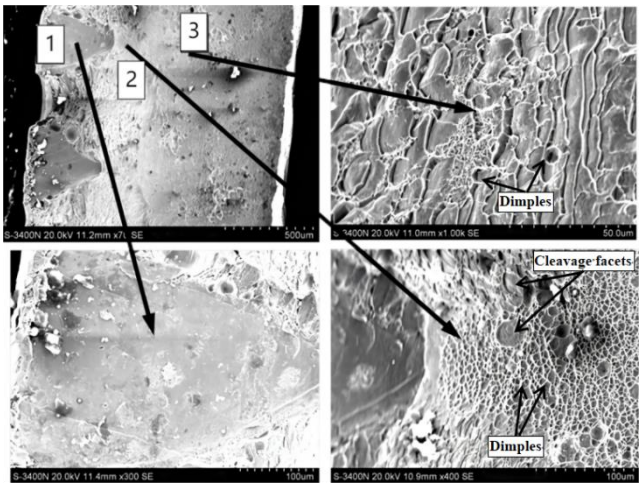

Fig. 12. Fracture morphologies of tensile specimens with a heat input of 2.125 kJ/cm

As shown in Fig. 13, the weld was basically permeable, and position 1 was the form of ferrite fracture in the WM.

The softening zone shows the grain characteristics in position 2. There were many equiaxial dimples in position 3, with good toughness.

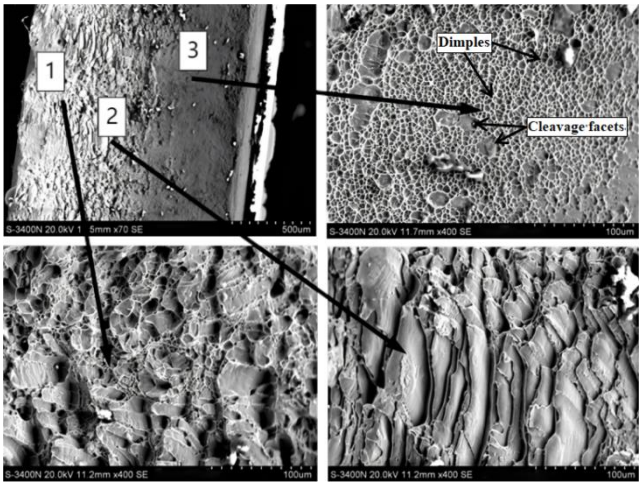

Fig. 13. Fracture morphologies of tensile specimens with a heat input of 2.67 kJ/cm

3. CONCLUSIONS

1. Reasonable laser welding parameters are essential for the macroscopic morphology of the welding of DSS. For 1.5 mm thickness plates, the optimal laser welding process parameters were a welding speed of 6 mm/s, laser power of 1.6 kW and welding speed of 8 mm/s, laser power of 1.7 kW.
2. By analyzing the microstructure of welded joints, we found that the ferrite in the weld mainly had two forms: columnar crystal and equiaxed crystal. Rod and granular Cr_2N were precipitated in the crystal. The austenite was mainly located at the grain boundary. With the increase of heat input, the ferritic grains grew along the fusion line toward the center, the long grain grew obviously, and the continuity of austenite increased at the grain boundary. When the heat input was 2.125 kJ/cm, the content of ferrite and austenite was relatively uniform, and the ratio was close to 1:1.
3. The hardness of WM was slightly higher than that of the base metal, with an average value of 330 HV. The hardness of HAZ was the smallest, with an average value of 280 HV. When the heat input was 2.125 kJ/cm, the microhardness of welded joint was obviously better than other parameters, reaching 400 HV in the WM. With the increase of heat input, the weld was gradually penetrated and the tensile resistance of the welded joint was enhanced. When the heat input was greater than 2.67 kJ/cm, the weld with good tensile performance could be obtained, and the maximum tensile strength was 900 MPa.
4. The fracture position of the tensile specimen was all in the weld zone, and there were a lot of dimples characteristics in the fracture morphology, which belongs to the ductile fracture.

Acknowledgements

We acknowledge the financial support of this work under the Key Scientific Research Project of Higher Education Institutions in Henan Province (Item Number:23B460029).

REFERENCES

1. **Varbai, B., Adonyi, Y., Baumer, R., Pickle, T., Dobranszky, J., Majlinger, K.** Weldability of Duplex Stainless Steels-thermal Cycle and Nitrogen Effects Duplex Stainless Steel Weld Microstructures Were Investigated as a Function of Weld Thermal Cycles and Shielding Gas Nitrogen Content *Welding Journal* 98 (3) 2019: pp. 78 – 87. https://doi.org/10.29391/2019.98.006
2. **Labanowski, J., Strzelczyńska, K.P., Rogalski, G., Fydrych, D.** The Effect of Wet Underwater Welding on Cold Cracking Susceptibility of Duplex Stainless Steel *Advances in Materials Science* 16 (2) 2016: pp. 68 – 77. https://doi.org/10.1515/adms-2016-0010
3. **Wang, K., Shao, C.L., Jiao, X.D., Zhu, J.L., Cai, Z.H., Li, C.W.** Investigation on Microstructure and Properties of Duplex Stainless Steel Welds by Underwater Laser Welding with Different Shielding Gas *Materials* 14 (17) 2021: pp. 4774 – 4776. https://doi.org/10.3390/ma14174774
4. **Zhang, P., Pang, W.J., Shang, F., Li, H.Q.** Research Status of Corrosion Resistance of SAF 2507 Super Duplex Stainless Steel *Hot Working Technology* 47 (14) 2018: pp.23 – 26. https://doi.org/10.14158/j.cnki.1001-3814.2018.14.006
5. **Cheng, X.Q., Wang, Y., Li, X.G., Dong, C.F.** Interaction between Austein-ferrite Phases on Passive Performance of 2205 Duplex Stainless Steel *Journal of Materials Science and Technology* 34 (11) 2018: pp. 2140 – 2148. https://doi.org/10.1016/j.jmst.2018.02.020
6. **Makhdoom, M.A., Ahmad, A., Kamran, M., Abid, K., Haider. W.** Microstructural and Electrochemical Behavior of 2205 Duplex Stainless Steel Weldments *Surfaces and Interfaces* 9 2017: pp. 189 – 195. https://doi.org/10.1016/j.surfin.2017.09.007
7. **Ramkumar, K.D., Mishra, D., Raj, B.G., Vignesh, M.K., Thiruvengatam, G., Sudharshan, S.P., Arivazhagan, N., Sivashanmugam, N., Rabel, A.M.** Effect of Optimal Weld Parameters in the Microstructure and Mechanical Properties of Autogeneous Gas Tungsten Arc Weldments of Super-duplex Stainless Steel UNS S32750 *Materials & Design* 66 2015: pp. 356 – 365. https://doi.org/10.1016/j.matdes.2014.10.084
8. **Cervo, R., Ferro, P., Tiziani, A.** Annealing Temperature Effects on Super Duplex Stainless Steel UNS S32750 Welded Joints. I: Microstructure and Partitioning of Elements *Journal of Materials Science* 45 (16) 2010: pp. 4369 – 4377. https://doi.org/10.1007/s10853-010-4310-1
9. **Zhan, Z.Y., Zhang, H.Z., Hu, J., Qi, X.X., Bian, Y., Shen, A., Xu, P.P., Zhao, Y.Q.** Microstructure Evolution and Mechanical Properties of Briefly Heat-treated SAF 2507 Super Duplex Stainless Steel Welds *Construction and Building Materials* 168 2018: pp. 338 – 345. https://doi.org/10.1016/j.conbuildmat.2018.02.143
10. **Singh, A., Singh, R.P.** A Review of Effect of Welding Parameters on the Mechanical Properties of Weld in

Submerged Arc Welding Process *Materials Today: Proceedings* 26 2020: pp. 1714 – 1717. https://doi.org/10.1016/j.matpr.2020.02.361

11. **Hong, J.F., Tan, H., Chen, L.D., Li, J., Jiang, Y.M.** Microstructure and Pitting Resistance of UNS S32304 Duplex Stainless Steel Plasma Arc Welding Joint *Acta Metallurgica Sinica* 47 (11) 2011: pp. 1445 – 1449. https://doi.org/10.3724/SP.J.1037.2011.00314
12. **Taban, E.** Toughness and Microstructural Analysis of SuperDuplex Stainless steel Joined by Plasma Arc Welding *Journal of Materials Science* 43 (12) 2008: pp. 4309 – 4315. https://doi.org/10.1007/s10853-008-2632-z
13. **Taban, E., Kaluc, E.** Welding Behaviour of Duplex and Superduplex Stainless Steels using Laser and Plasma Arc Welding Processes *Welding in the World* 55 (7 – 8) 2011: pp. 48 – 57. https://doi.org/10.1007/BF03321307
14. **Ramkumar, K.D., Mishra, D., Vignesh, M.K., Raj, B.G., Arivazhagan, N., Naren, S.V., Kumar, S.S.** Metallurgical and Mechanical Characterization of Electron Beam Welded Super-duplex Stainless Steel UNS 32750 *Journal of Manufacturing Processes* 16 (4) 2014: pp. 527 – 534. https://doi.org/10.1016/j.jmapro.2014.07.011
15. **Kolenic, F., Kovac, L., Drimal, D.** Effect of Laser Welding Conditions on Austenite/Ferrite Ratio in Duplex Stainless Steel 2507 Welds *Welding in the World* 55 (5 – 6) 2011: pp. 19 – 25. https://doi.org/10.1007/BF03321292
16. **Metelkova, J., Kinds, Y., Kempen, K., Formanoir, C.D., Witvrouw, A., Hooreweder, B.V.** On the Influence of Laser Defocusing in Selective Laser Melting of 316L *Additive Manufacturing* 23 2018: pp. 161 – 169. https://doi.org/10.1016/j.addma.2018.08.006
17. **Saravanan, S., Raghukandan, K., Sivagurumanikandan, N.** Pulsed Nd: YAG Laser Welding and Subsequent Post-weld Heat Treatment on Super Duplex Stainless Steel *Journal of Manufacturing Processes* 25 2017: pp. 284 – 289. https://doi.org/10.1016/j.jmapro.2016.12.015
18. **Chen, Y., Liu, T.M., Lu, L.W., Zhang, Z.C.** Thermally Diffused Antimony and Zinc Coatings on Magnesium Alloys AZ31 *Surface Engineering* 28 (5) 2012: pp. 382 – 386. https://doi.org/10.1179/1743294411Y.0000000019
19. **Haghdadi, N., Laleh, M., Chen, H.S., Chen, Z.B., Ledermueller, C., Liao, X.Z., Ringer, S., Primig, S.** On the Pitting Corrosion of 2205 Duplex Stainless Steel Produced by Laser Powder Bed Fusion Additive Manufacturing in the As-built and Post-processed Conditions *Materials & Design* 212 2021: pp. 693 – 703. https://doi.org/10.1016/j.matdes.2021.110260
20. **Liu, Q.H., Xu, Y.L., Yao, J.** Effect of Aging Treatment at 750 ℃ on Microstructure and Mechanical Properties of a New Si-Bearing Duplex Stainless Steel *Shanghai Metal* 38 (5) 2016: pp. 33 – 38.
21. **Yang, W., Wang, X.H., Zhang, L.F., Wang, W.J.** Characteristics of Alumina-based Inclusions in Low Carbon Al-killed Steel Under No-stirring Condition *Steel Research International* 84 (9) 2013: pp. 878 – 891. https://doi.org/10.1002/srin.201200271
22. **Gao, Z.J., Li, J.Y., Chen, Y.L., Wang, Y.D.** Effect of Dual-phase Structure on the Microstructure and Deformation in Homogeneity of 2507 Duplex Stainless Steel *Ironmaking and Steelmaking* 48 (4) 2021: pp. 393 – 401. https://doi.org/10.1080/03019233.2020.1794766
23. **Habibi, N., Zarei, A.H., Abedi, H.R.** An Investigation into the Fracture Mechanisms of Twinning-induced-plasticity Steel Sheets under Various Strain Path *Journal of Materials Processing Technology* 224 2015: pp. 102 – 116. https://doi.org/10.1016/j.jmatprotec.2015.04.014
24. **Shao, C.L., Zhu, J.L., Mei, L., Wang, K., Li, C.W., Miao, C.Y. Zhu, Y.Y.** Study on Laser Wire Filling Welding Process and Weld Properties of S32101 Duplex Stainless Steel *Applied Laser* 41 (5) 2021: pp. 943 – 947. https://doi.org/10.14128/j.cnki.al.20214105.943
25. **Wang, H.T., Bi, Z.Y., Liu, Y.D., Wang, W.D.** Performance Analysis of Duplex Stainless Steel Laser Welding Joint *Applied Laser* 40 (1) 2020: pp. 56 – 61. https://doi.org/10.14128/j.cnki.al.20204001.056
26. **Li, G.Z., Li, R.F., Ye, X.N., Liu, X.D., Wu, M.F.** Study on Microstructure and Corrosion Resistance of Laser Welded Joint of 2507 Super Duplex Stainless Steel *Welding Technique* 46 (12) 2017: pp. 8 – 11. https://doi.org/10.13846/j.cnki.cn12-1070/tg.2017.12.003
27. **Liao, F., Wang, M.Q., Tu, L.S., Wang, J., Lu, L.F.** Micromechanical Fracture Model Parameter Influencing Factor Study of Structural Steels and Welding Materials *Construction And Building Materials* 8 (215) 2019: pp. 898 – 917. https://doi.org/10.1016/j.conbuildmat.2019.04.155
28. **Feng, Y.L., Li, R.** Study on Welding and Heat Treatment Process of 2507 Super Duplex Stainless Steel *Welded Pipe* 41 (5) 2018: pp. 14 – 19. https://doi.org/10.19291/j.cnki.1001-3938.2018.05.003